remote sensing

Article

Clutter and Interference Cancellation in River Surface Velocity Measurement with a Coherent S-Band Radar

Yichen Zeng, Zezong Chen *, Chen Zhao, Yunyu Wei and Jiangheng He

School of Electronic Information, Wuhan University, Wuhan 430072, China
* Correspondence: chenzz@whu.edu.cn; Tel.: +86-133-0711-8527

Abstract: Using a Doppler radar to measure river surface velocity is a safe and effective technique. However, the measurement would be severely affected by undesired targets that enter the illuminated area of radar. The issue is worsened when measuring the surface velocities of wide rivers because undesired targets such as boats and ships are more likely to be present. The buoy boats fixed on the river surface and cargo ships sailing on the river would generate ground clutter and moving target interference, respectively. The clutter and interference can mask the signal produced by the Bragg scattering and seriously bias the extraction result of river surface velocity. This paper proposes two effective methods to remove ground clutter and moving target interference, respectively. One is an improved phase-based method that eliminates ground clutter after obtaining its boundaries through the phase in the frequency domain, and another is an improved constant false alarm rate (CFAR) detector that combines smallest-of selection logic and a multi-step deletion scheme to detect and remove interference in the time-Doppler spectrum. The experimental data measuring the surface velocity of the Yangtze River with a coherent S-band radar in July 2022 are used to verify the proposed methods. The results show that the proposed methods can effectively remove ground clutter and moving target interference, respectively. After clutter and interference cancellation, a more reasonable result of river surface velocity distribution can be extracted. Therefore, the methods proposed in this paper can be used to remove clutter and interference when extracting the surface velocity of rivers with numerous undesired targets.

Keywords: Doppler radar; coherent S-band radar; river surface velocity; Bragg scattering; ground clutter; moving target interference; CFAR detector

Citation: Zeng, Y.; Chen, Z.; Zhao, C.; Wei, Y.; He, J. Clutter and Interference Cancellation in River Surface Velocity Measurement with a Coherent S-Band Radar. *Remote Sens.* **2023**, *15*, 3979. https://doi.org/10.3390/rs15163979

Academic Editor: Alfonso Vitti

Received: 9 July 2023
Revised: 1 August 2023
Accepted: 8 August 2023
Published: 11 August 2023

1. Introduction

A Doppler radar measures the river surface velocity through the Doppler shift induced by the electromagnetic waves backscattered from the rough water surface [1,2]. Then, cross-sectional velocity distribution [3,4] or mean velocity [5] can be obtained according to the principle of fluid dynamics. Finally, the river discharge is estimated using the velocity area method [6]. Compared with conventional contact measurement instruments such as acoustic Doppler current profilers (ADCPs) [7,8], Doppler radars have the advantages of noncontact with water bodies, and can provide safe and real-time measurement in all weather conditions [9].

Since river monitoring plays a critical role in flood prevention and disaster mitigation, different radar systems have been developed to monitor rivers. For example, the UHF-band radar system RiverSonde [10–12], the K-band sensor Riverscat, the X-band radar system RiverRad [5,13,14], and the UHF-band radar system OSMAR-SU [15,16]. The basis of these radar systems for measuring rivers is similar, with the exception that Bragg scattering occurs with different wavelengths of water waves.

The previous studies on river monitoring concentrated on small or medium-sized rivers which have few undesired targets. When measuring the surface velocities of wide rivers, undesired targets are more frequently present, such as buoy boats and cargo ships.

Buoy boats fixed on the river surface generate ground clutter, and cargo ships sailing on the river generate moving target interference. The clutter and interference can mask the signal produced by the Bragg scattering and cause great trouble for surface velocity extraction. Hence, it is necessary to adopt effective methods to remove the clutter and interference in order to extract the river surface velocity accurately.

Ground clutter from stationary targets has a zero-mean frequency and narrow spectrum width, which is common in various radar systems. Different time and frequency domain filters were designed to eliminate ground clutter [17–19]. However, these filters require prior knowledge of ground clutter, such as spectrum width, intensity, etc. The performance of these filters is degraded when the characteristics of ground clutter change. Therefore, many novel methods have been proposed to eliminate ground clutter. Warde and Torres introduced an approach to analyzing weather signals using autocorrelation spectral density (ASD) [20] and then proposed a CLEAN-AP filter to remove ground clutter from weather signals [21]. Golbon-Haghighi et al. proposed a method using the phase fluctuation index (PFI) [22]. Wang et al. used eigenvalue decomposition (EVD) to distinguish meteorological signals from ground clutter [23]. Bachmann et al. proposed a phase-based method [24], which removed ground clutter after obtaining a spectral mask through the phase in the frequency domain. However, the threshold of the spectral mask was determined empirically. For this reason, this paper proposes an improved phase-based method based on the research of Bachmann et al., which gives determination criteria to get the correct boundaries of ground clutter.

Moving target interference can first be detected and then removed. Using a constant false alarm rate (CFAR) detector is a common method to detect moving targets. Due to the high resolution of radars, the echoes generated by cargo ships would severely extend in the Doppler spectrum. Using a conventional CFAR detector can lead to serious masking effects. To alleviate the masking effects, Weiss proposed a smallest-of (SO)-CFAR detector [25]. Barboy et al. proposed a censoring scheme to address the multiple interfering targets scenario [26]. Xu et al. used an improved SO-CFAR detector to alleviate the masking effects by replacing the detected targets with noise [27]. Zhang et al. used energy accumulation and ordered statistical (OS)-CFAR detector to detect Doppler-spread targets [28]. Kuang et al. proposed a 3-dimensional cell-averaging (CA)-CFAR detector for detecting ships in rivers [29], but it may suffer from the masking effects. Therefore, this paper proposes an improved CFAR detector combining smallest-of selection logic and a multi-step deletion scheme. The detector can quickly and effectively detect and remove moving target interference in the time dimension of the time-Doppler spectrum.

The experimental data measuring the surface velocity of the Yangtze River with a coherent S-band radar in July 2022 are used to verify the methods proposed in this paper. The results show that the methods have excellent performance in clutter and interference cancellation, leading to a more reasonable extraction result of river surface velocity.

The structure of this paper is as follows. Section 2 first introduces the principle of radar measurement of river surface velocity, then presents the extraction process of river surface velocity and proposes methods to remove ground clutter and moving target interference. Section 3 verifies the effectiveness of the proposed methods using experimental data. Section 4 compares the extraction results of river surface velocity before and after clutter and interference cancellation and discusses the limitations of the proposed methods. Section 5 concludes the paper.

2. Materials and Methods

2.1. Measurement Principle

A Doppler radar is deployed on the river bank to measure the river surface velocity distribution, as shown in Figure 1. The resonance condition of the first-order Bragg scattering from the rough river surface [1,30] is

$$\lambda_B = \frac{\lambda}{2\cos\beta} \tag{1}$$

where λ_B is the wavelength of the resonant water wave (the Bragg wave), and λ is the wavelength of the electromagnetic wave.

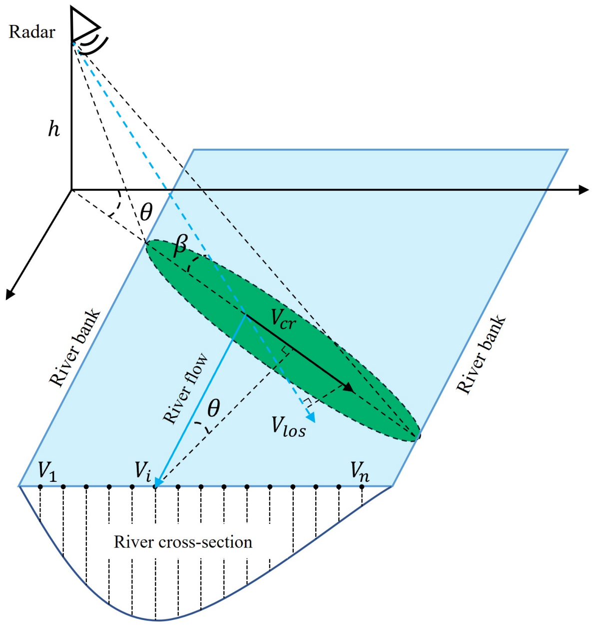

Figure 1. Schematic diagram of radar measuring river surface velocity distribution. In the figure, V_i is the surface velocity of the ith range cell on the river, and V_{cr} and V_{los} are the radial velocity and line-of-sight velocity of V_i relative to the radar, respectively. The height of the radar over the river surface is h. The grazing angle to the illuminated water surface is β, and the angle with the cross direction of the river is θ. The green ellipse area indicates the illuminated area of radar. β is close to 0, and θ is typically 20∼50° for the field measurement.

The Doppler shift generated by Bragg scattering [30] is

$$f_B = \frac{V_p}{\lambda_B} = \sqrt{\frac{g}{2\pi\lambda_B} + \frac{2\pi\gamma}{\lambda_B^3}} \tag{2}$$

where V_p is the phase velocity of the Bragg wave, g is the acceleration of gravity, γ is the surface tension of water, and γ = 74 cm^3/s^2. For an S-band radar, the wavelength of the Bragg wave is about 5 cm under grazing conditions, and the Doppler shift f_B is about 6 Hz.

Only the Bragg waves traveling toward or away from the radar are effective scatterers. Thus, when the river flows relative to the radar, the Doppler shift can be expressed as [1,30]:

$$f_d = \frac{2V_{los}}{\lambda} = \frac{2\left(V_{cr} \pm V_p\right)\cos\beta}{\lambda} = f_{cr} \pm f_B \tag{3}$$

where f_{cr} is the Doppler shift caused by the surface velocity V_{cr} of the river. f_{cr} is positive when the river flows toward the radar, while f_{cr} is negative when the river flows away from the radar.

Two Bragg peaks induced by the Bragg waves appear in the Doppler spectrum: the positive Bragg peak with a frequency of $f_p = f_{cr} + f_B$ and the negative Bragg peak with a frequency of $f_n = f_{cr} - f_B$ [1,30]. f_{cr} can be obtained from the frequencies of the two Bragg peaks [31]:

$$f_{cr} = \frac{f_p + f_n}{2}. \tag{4}$$

Assuming that the flow in a straight river is uniform and ignores the cross-channel flow [32]. Then, V_i is given by

$$V_i = \frac{V_{cr}}{\sin\theta} \tag{5}$$

The surface velocity of the ith range cell on the river is calculated as

$$V_i = \frac{V_{los}}{\sin\theta\cos\beta} = \frac{cf_{cr}}{2f_0\sin\theta\cos\beta} \tag{6}$$

where f_0 is the transmitting frequency of the radar. By extracting the surface velocities of all range cells from Doppler spectra, the surface velocity distribution over the entire river can be obtained.

2.2. Methods

The extraction flowchart of river surface velocity is shown in Figure 2, and the specific steps are as follows.

Step 1: Use multiple pulses of the same range cell to remove ground clutter and obtain the Doppler spectrum. Ground clutter is highly correlated in time, which is not the case for noise. The boundaries of ground clutter are obtained through their phase differences in the frequency domain. Then use the boundaries to remove ground clutter [24]. The detailed process is as follows.

(1) Obtain the sequence $x(n)$ from the same range cell after $2N$ sweep periods and divide it into an even sequence x_{even} and an odd sequence x_{odd}:

$$x_{even} = x(2n) \qquad x_{odd} = x(2n+1) \tag{7}$$

where $n = 0, 1, 2, \ldots, N-1$.

(2) Apply a Hanning window and discrete Fourier transform (DFT) to obtain the spectrum S, S_{even}, and S_{odd} of the sequence $x(n)$, even sequence x_{even}, and odd sequence x_{odd}, respectively:

$$S(k) = \sum_{n=0}^{2N-1} x(n) W_{2N}^{kn} \tag{8}$$

where k is the discrete frequency, and $k = 0,\ 1,\ 2, \ldots,\ 2N-1$, $W_{2N}^{kn} = e^{-j2\pi kn/2N}$;

$$S_{even}(k) = \sum_{n=0}^{N-1} x(2n) W_N^{kn} \tag{9}$$

$$S_{odd}(k) = \sum_{n=0}^{N-1} x(2n+1) W_N^{kn} \tag{10}$$

where $k = 0, 1, 2, \ldots, N-1$, $W_N^{kn} = e^{-j2\pi kn/N}$.

(3) Calculate the parameter:

$$\phi_0(k) = arg[S_{even}(k) S_{odd}^*(k)] \tag{11}$$

where arg means taking the phase and * means complex conjugation. Since ground clutter is strongly correlated in time, $x(2n+1)$ can be regarded as the sequence obtained after $x(2n)$ lagged by one sampling interval. Thus, Equation (10) can be rewritten as

$$S_{odd}(k) = W_{2N}^{k} \sum_{n=0}^{N-1} x(2n) W_N^{kn} = W_{2N}^{k} S_{even}(k) \tag{12}$$

according to the circular time-shifting theorem of DFT, and

$$\phi_0(k) = arg[S_{even}(k) W_{2N}^{-k} S_{even}^*(k)] = arg[W_{2N}^{-k} |S_{even}(k)|^2] = \frac{k\pi}{N}. \tag{13}$$

For noise, sequences $x(2n)$ and $x(2n+1)$ have a very low correlation, and $\phi_0(k)$ can be considered random.

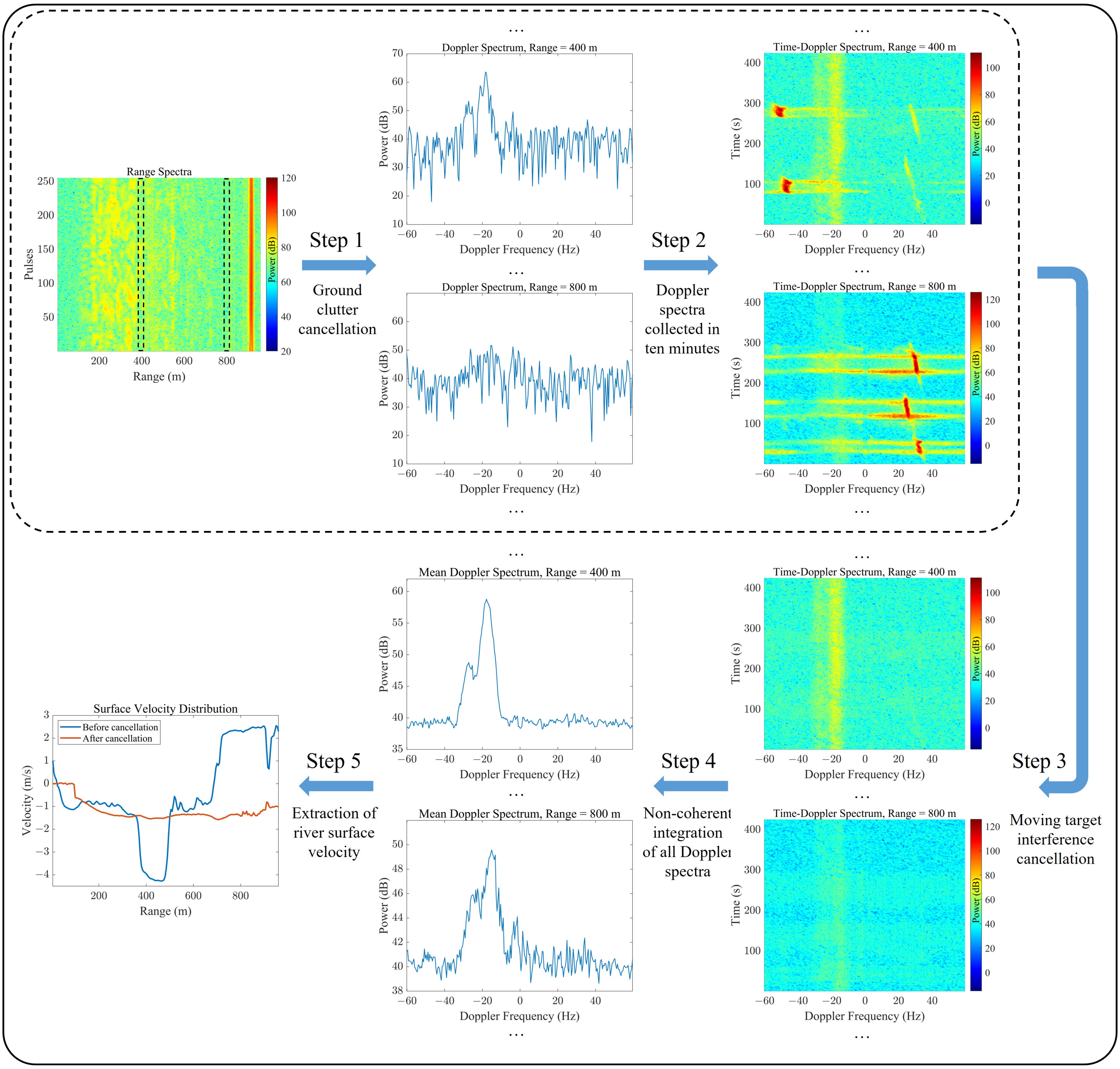

Figure 2. Extraction flowchart of river surface velocity.

(4) Obtain the parameter $\Delta\phi_0(k)$ by taking a central difference for $\phi_0(k)$. For ground clutter,

$$\Delta\phi_0(k) = \frac{\phi_0(k+1) - \phi_0(k-1)}{2} = \frac{\pi}{N} \tag{14}$$

is a constant, where $k = 1, 2, 3, \ldots, N-2$. For noise, $\Delta\phi_0(k)$ can also be considered random.

(5) Get the boundaries of ground clutter using the determination criteria:

$$T_1 < \Delta\phi_0(k) < T_2. \tag{15}$$

The threshold values T_1 and T_2 are calculated as follows:

$$T_1 = (-a+1)\frac{\pi}{N} \qquad T_2 = (a+1)\frac{\pi}{N} \tag{16}$$

where a is the product factor. The first value of k that does not satisfy the criteria is found from zero to the left/right as the left/right boundary of ground clutter, respectively, as shown in Figure 3.

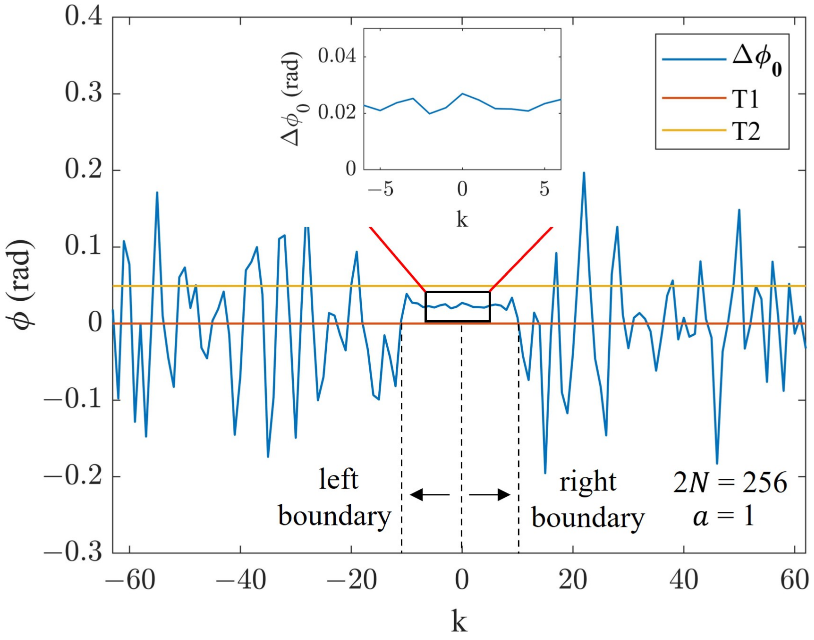

Figure 3. Schematic diagram to get the left and right boundaries of ground clutter using simulated data. The number of pulses is 256, and the calculated $\Delta\phi_0$ in the ground clutter region is close to the theoretical value of 0.0245.

(6) Remove the components in the spectrum S between the boundaries, and then fill in the removed components using noise. The value of the parameter $\Delta\phi_0$ in the ground clutter region is only related to the number of pulses $2N$ and independent of the spectrum width of ground clutter and other radar parameters. It changes from a small constant to a random value at the boundaries between ground clutter and noise. Thus, the boundaries of ground clutter can be obtained easily. While in a field experimental environment, ground clutter is exposed to phase errors, and the value of the parameter $\Delta\phi_0$ fluctuates. Therefore, it is necessary to use the product factor a to get the appropriate threshold values T_1 and T_2 to ensure that the correct boundaries are obtained. The value of the product factor a depends on the severity of phase errors, and the recommended values are 2 to 6.

Step 2: The Doppler spectra collected at the same range cell in ten minutes are composed of one time-Doppler spectrum. In the presence of ground clutter and moving target interference, a typical time-Doppler spectrum is shown in Figure 4. It can be seen that when the cargo ships enter or exit the illuminated area of radar, the moving target interference is severely extended in the frequency domain. The complex bow and stern of the cargo ships may cause this phenomenon. The frequency cells occupied by the Bragg peaks are relatively stable in the time dimension, while the moving target interference only lasts for a short time.

Step 3: Detect and remove moving target interference using a CFAR detector in the time dimension of the time-Doppler spectrum. The long length of cargo ships results in a long time to be illuminated by radar. Therefore, the echoes of cargo ships occupy many time cells in the time dimension and cannot be treated as point targets.

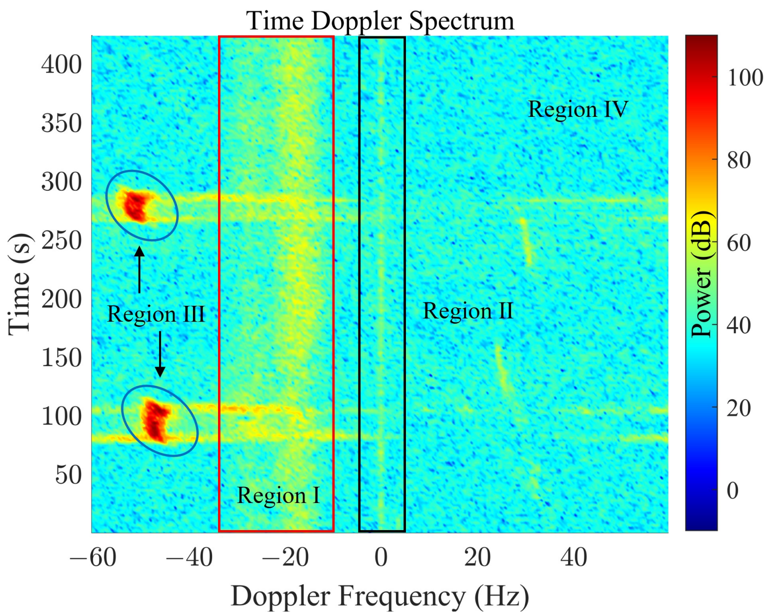

Figure 4. A typical time-Doppler spectrum. It can be roughly divided into four regions: Region I, shown by the red rectangle, indicates the Bragg peaks generated by water waves. Region II, shown by the black rectangle, indicates ground clutter generated by buoy boats. Region III, shown by the blue ellipse, indicates moving target interference generated by cargo ships. The remaining region is Region IV, which indicates noise.

This paper proposes an improved CFAR detector combining a smallest-of selection logic (SO) and a multi-step deletion scheme to detect and remove moving target interference. The block diagram of the CFAR detector is shown in Figure 5. The hypotheses of H_0 and H_1 are as follows:

$$\begin{aligned} H_0 &: s(t) = b(t) + n(t) \\ H_1 &: s(t) = i(t) + b(t) + n(t) \end{aligned} \tag{17}$$

where $i(t)$, $b(t)$, and $n(t)$ denote the components of moving target interference, Bragg peaks, and noise, respectively.

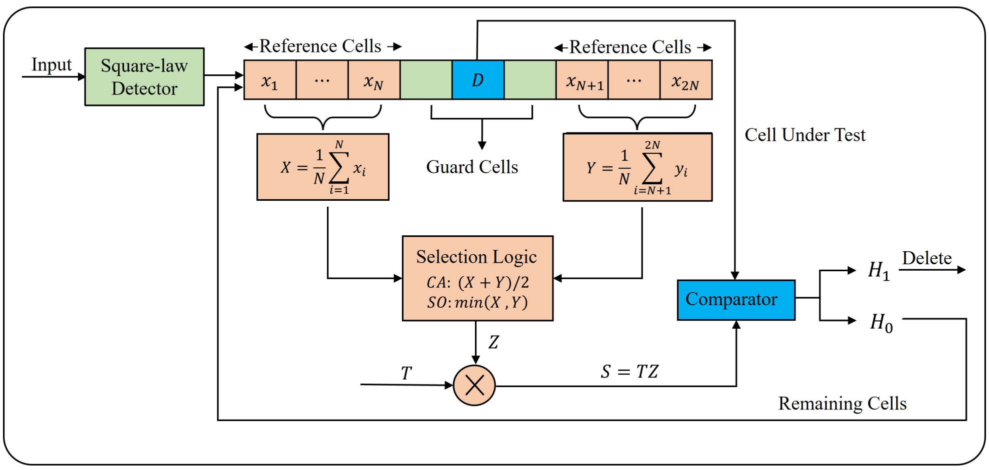

Figure 5. Block diagram of the improved CFAR detector.

The time series of a frequency cell in the time-Doppler spectrum is the input of the CFAR detector. The detailed process is as follows.

(1) Obtain the threshold product factor T according to the false alarm rate P_{fa} and the number of reference cells $2N$. The false alarm probability P_{fa} of the detector is [27]:

$$P_{fa} = 2\sum_{i=0}^{N-1}\binom{N+i-1}{i}(2+T)^{-(N+i)}. \tag{18}$$

As a result, the threshold product factor T cannot be calculated directly. However, from the given false alarm probability P_{fa} and number of reference cells $2N$, the threshold product factor T can be approximated.

(2) Estimate the noise power level Z, then detect and mark the positions of all time cells that are larger than the decision threshold S;

(3) Delete all the marked time cells at the end of detection;

(4) Repeat steps 2 and 3 using the remaining time cells until all time cells larger than the decision threshold S is deleted;

(5) Estimate the parameters of the remaining time cells to restore all the deleted time cells.

After processing all the frequency cells, the detector completes the cancellation of moving target interference in the time-Doppler spectrum. The detector combines the smallest-of selection logic and the multi-step deletion scheme to detect and remove moving target interference quickly and effectively. The number of reference cells and the false alarm rate P_{fa} must be carefully selected. An appropriate false alarm rate allows the detector to remove as much moving target interference as possible without excessively removing other echoes.

Step 4: Obtain the mean Doppler spectrum by non-coherent integration. Assuming that the flow in a straight river is uniform without external disturbances and the river surface velocity does not change in a short time. The mean Doppler spectrum can be obtained by

$$S_m(f) = \frac{1}{M}\sum_{i=1}^{M} S_i(f) \tag{19}$$

where M is the number of Doppler spectra undergoing non-coherent integration, $S_i(f)$ is the collected Doppler spectrum, and $S_m(f)$ is the mean Doppler spectrum obtained after non-coherent integration. Since ground clutter and moving target interference can seriously affect the effectiveness of non-coherent integration, they must be removed before this step. It can be seen from Figure 2 that the SNR of the Bragg peaks is significantly improved after non-coherent integration.

Step 5: Extract the river surface velocity distribution. Estimate the centroid frequency of the mean Doppler spectrum as the Doppler shift f_{cr} using the spectral moment method [32,33] (ignoring the effect of different intensities of positive and negative Bragg peaks):

$$f_{cr} = \frac{\int_{f_L}^{f_R} f S_m(f)df}{\int_{f_L}^{f_R} S_m(f)df} \tag{20}$$

where f is the Doppler frequency, f_L and f_R are the left and right boundaries of the Bragg peaks, respectively, and $S_m(f)$ is the mean Doppler spectrum. The estimation of the boundaries f_L and f_R is shown in Figure 6 [34].

Extract the river surface velocity at a specific range cell using Equations (6) and (20). The river surface velocity distribution can be obtained by performing the above operations for every range cell.

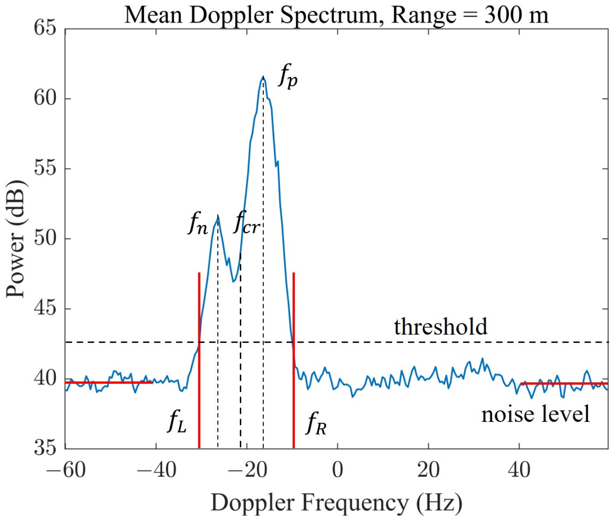

Figure 6. Schematic diagram of boundaries estimation of Bragg peaks. The noise level of the mean Doppler spectrum is first estimated, then a threshold of 3 dB higher than the noise level is obtained. Finally, the positions above the threshold are found as the boundaries of the Bragg peaks.

3. Results

3.1. Experiment Description

In June–July 2022, an experiment was conducted using a coherent S-band radar to measure the surface velocity of the Yangtze River near the Tianxingzhou Yangtze River Bridge in Qingshan District, Wuhan City. The coherent S-band radar is a modification of the microwave ocean remote sensor (MORSE) to monitor rivers [32].

The radar uses a frequency modulated interrupted continuous wave (FMICW) as the transmitting signal. The coherent integration time of the radar is

$$T = MT_0 \tag{21}$$

where M is the number of pulses for coherent integration, T_0 is the sweep period of the radar. The frequency resolution and velocity resolution of the radar can be expressed as follows:

$$\Delta f = \frac{1}{T} \tag{22}$$

$$\Delta v = \frac{c\Delta f}{2f_0}. \tag{23}$$

Therefore, the maximum radial velocity that the radar can measure is

$$v_{max} = \pm\frac{M\Delta v}{2} = \pm\frac{c}{4f_0T_0} \tag{24}$$

where f_0 is the transmitting frequency of the radar.

The radar parameters used in this experiment are shown in Table 1.

The experimental information is shown in Figure 7. The Yangtze River is extremely wide and rich in shipping resources. As a result, there are many buoy boats on the river surface, and cargo ships appear frequently at the experimental site.

The experimental data from 11:40 to 11:49 on July 26 are used to verify the effectiveness of the methods proposed in this paper. Since boats and ships have very high echo powers, the positions of maximum powers can be used to indicate their positions. The obtained distribution of boats and ships is shown in Figure 8.

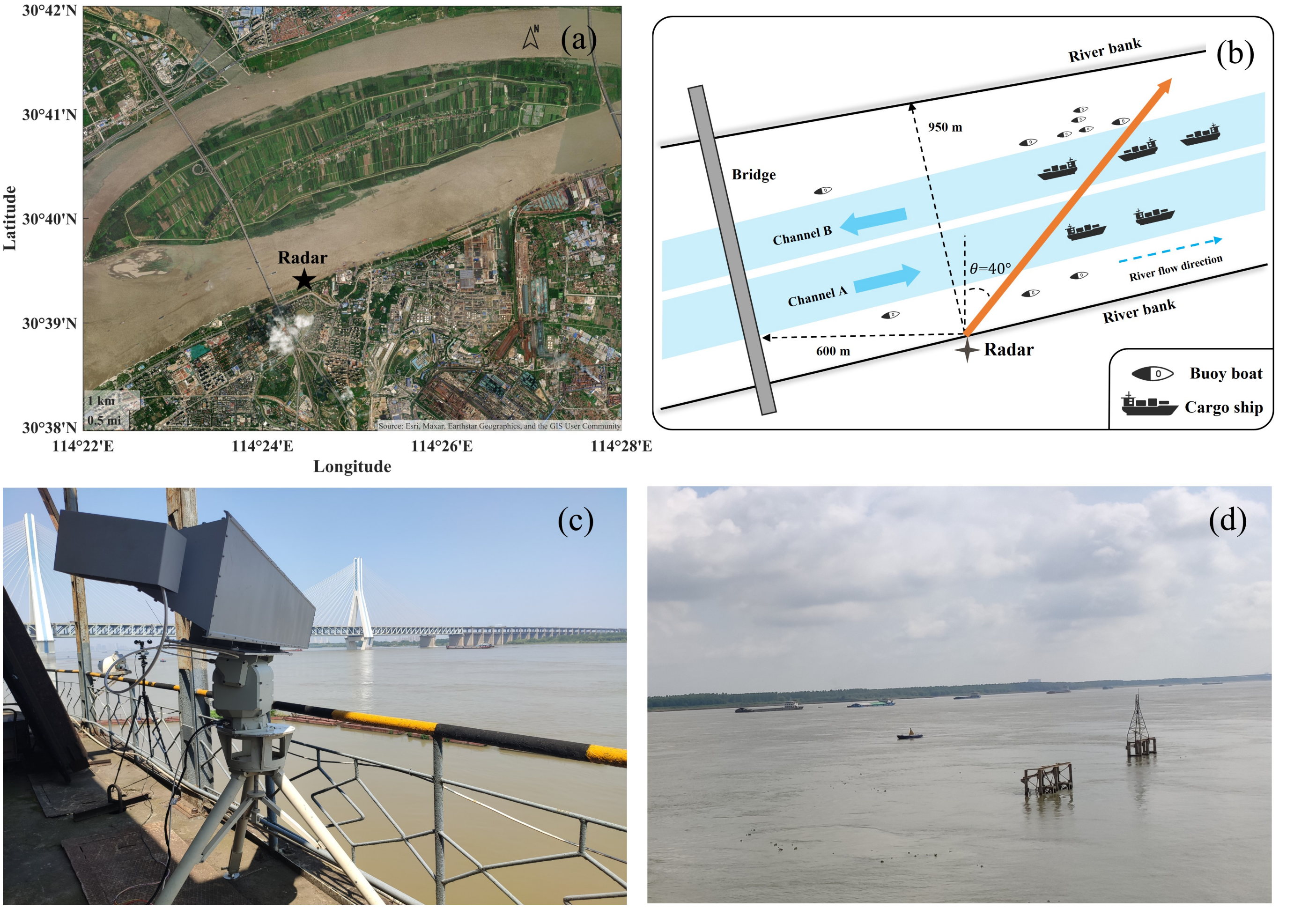

Figure 7. The experimental information: (**a**) shows the satellite view of the experimental site; (**b**) shows the overview of the river environment at the experimental site, the orange arrow indicates the illumination direction of the radar, and the blue dashed arrow shows the direction of the river flow, the blue background stripes indicate the ship channels, and the blue arrows show their directions; (**c**) shows the radar illuminating the surface of the Yangtze River; and (**d**) shows the river surface with buoy boats and cargo ships.

Table 1. Parameters of the coherent S-band radar.

Parameters	Values
Transmitting frequency	2.85 GHz
Transmitting power	5 W
Sweep bandwidth	30 MHz
Sweep period	8.32 ms
Range resolution	5 m
Coherent integration time	2.13 s
Velocity resolution	2.47 cm/s
Maximum radial velocity	±3.16 m/s
Polarization mode	VV
Antenna beamwidth	4.25° (horizontal) 23.89° (vertical)

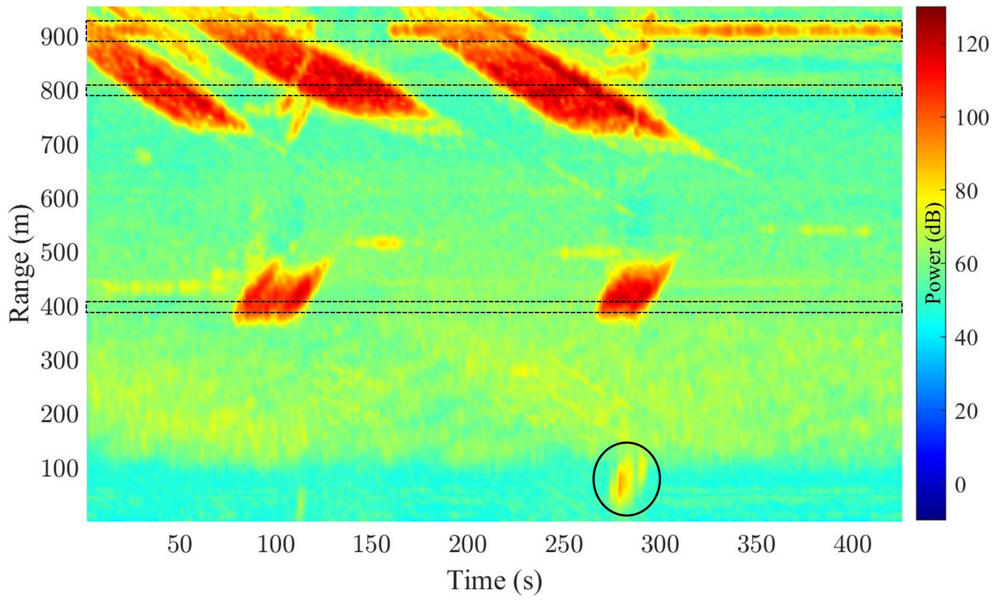

Figure 8. Distribution of boats and ships. It shows that two cargo ships appeared in channel A and three in channel B during the period. The black circle indicates the echoes of a patrol boat.

Ground clutter is affected by the distribution of buoy boats. As a consequence, the intensities of ground clutter vary at different range cells. The buoy boat at 920 m is located within the radar illumination area, which produces strong echoes. However, the other buoy boats deviate from the radar illumination area, producing relatively weak echoes. The presence of moving target interference depends on whether there are cargo ships entering the radar illumination area during the measurement. The time-Doppler spectra at 400 m (in channel A), 800 m (in channel B), and 920 m are selected to verify the effectiveness of the proposed methods, which are indicated by the black dashed rectangles in Figure 8.

3.2. Ground Clutter Cancellation

The results of ground clutter cancellation are shown in Figure 9. Figure 9a shows the time-Doppler spectrum at 920 m. Due to the obscuration by the three cargo ships in channel B, the radar can only receive ground clutter partially. Therefore, the spectrum widths of ground clutter at this range cell vary at different times. Figure 9b shows the parameter $\Delta\phi_0$ calculated by step 1 in Section 2.2. It can be seen that the parameter $\Delta\phi_0$ gives a good indication of the ground clutter region. Moving target interference is also highly correlated in time, with the value of the parameter $\Delta\phi_0$ similar to that of ground clutter. The length of the parameter $\Delta\phi_0$ is $N-2$, so the sampling frequency is approximately half of the Doppler spectrum (length of $2N$), resulting in the frequency collapsing in Figure 9b. It is difficult to extract the boundaries of moving target interference, so the improved phase-based method is not used to remove moving target interference. Since the calculated parameter $\Delta\phi_0$ has singular values in the ground clutter region because of phase errors, the product factor a is set to 4 in this paper. Ground clutter is then removed using the obtained boundaries, and the result is shown in Figure 9c. Figure 9d shows the result after noise filling.

The results show that the improved phase-based method can effectively distinguish and remove ground clutter with variable spectrum width, which shows strong robustness when only the number of pulses is known.

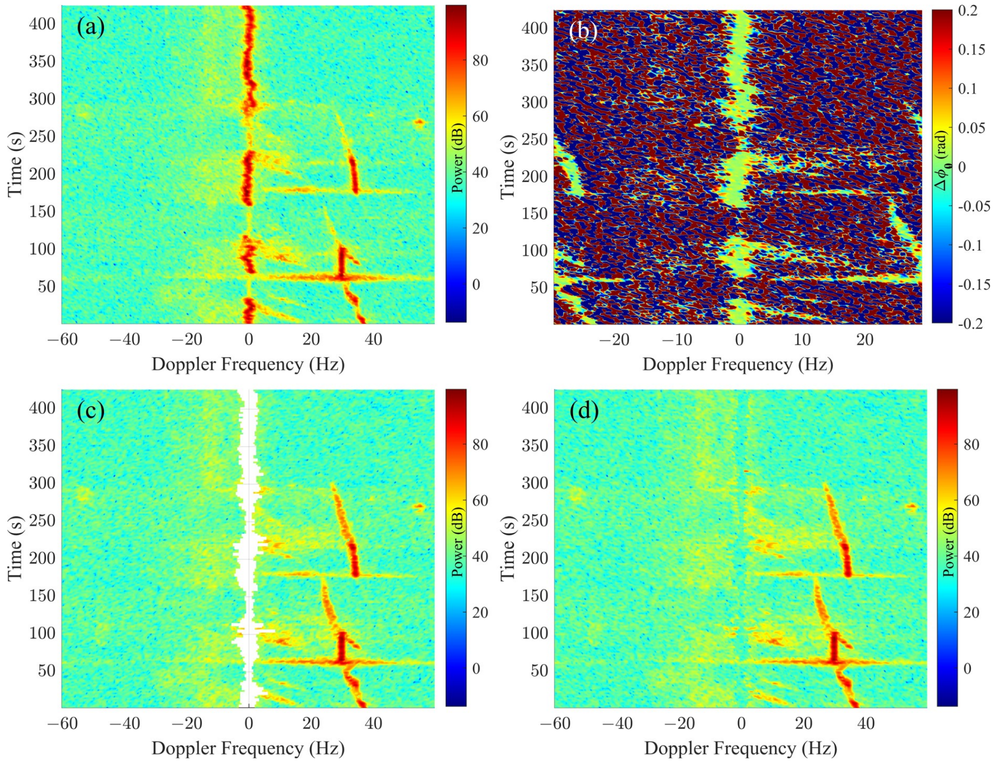

Figure 9. Ground clutter cancellation: (**a**) shows the time-Doppler spectrum before cancellation; (**b**) shows the calculated parameter $\Delta\phi_0$; (**c**,**d**) shows the results of ground clutter cancellation.

3.3. Moving Target Interference Cancellation

The number of reference cells is set to 32 and the number of guard cells is set to 4 in this paper. The curves of false alarm rate P_{fa} versus detection probability P_d under different interference-to-noise ratios (INRs) are shown in Figure 10. As seen from Figure 10, when the false alarm rate P_{fa} is equal to 0.01, the detector has a small P_d at a low INR, which does not excessively remove noise and Bragg peaks. While the detector has an excellent P_d at a high INR, allowing it to detect and remove moving target interference as much as possible. Therefore, this paper sets P_{fa} to 0.01.

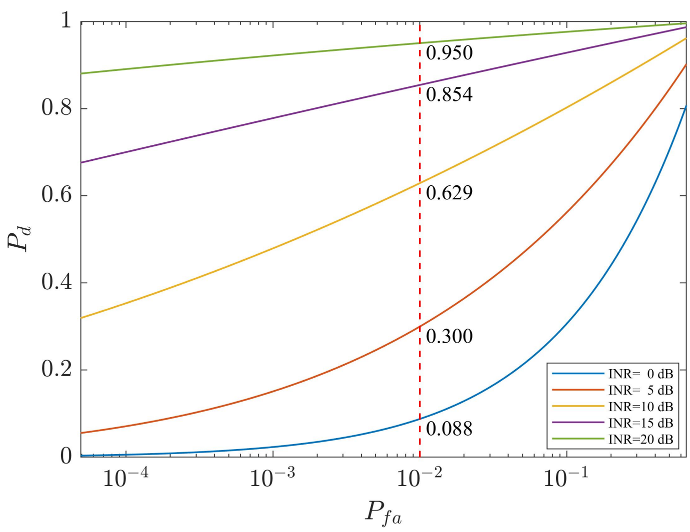

Figure 10. Curves of false alarm rate P_{fa} versus detection probability P_d under different interference-to-noise ratios (INRs).

The moving target interference cancellation results of the time-Doppler spectra at 800 m are shown in Figure 11. The moving target interference generated by the three cargo ships is severely extended in the time and Doppler dimensions and masks the Bragg peaks. After cancellation, the moving target interference is removed effectively while the Bragg peaks are preserved.

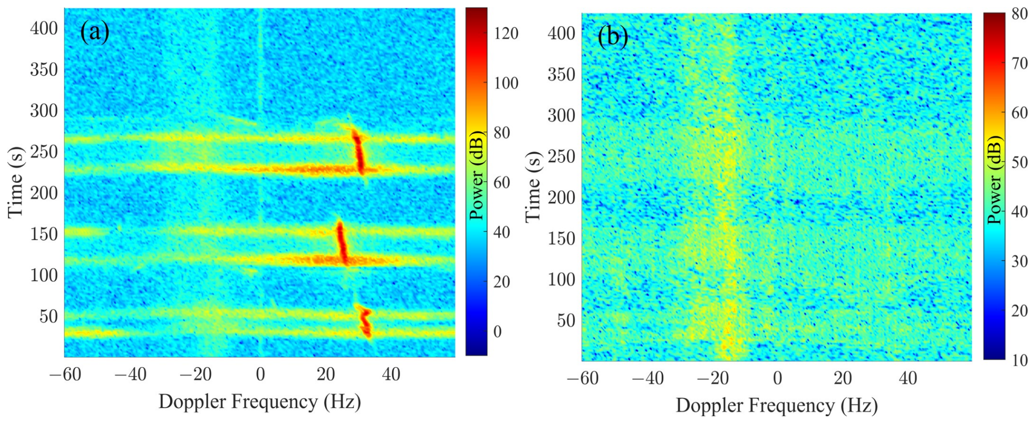

Figure 11. The cancellation results of moving target interference: (**a**,**b**) show the time-Doppler spectra at 800 m before and after moving target interference cancellation, respectively.

The interference cancellation process of the frequency cell f = 30.99 Hz is shown in Figure 12. The detector removes part of the moving target interference in each iteration and completes the cancellation after five iterations.

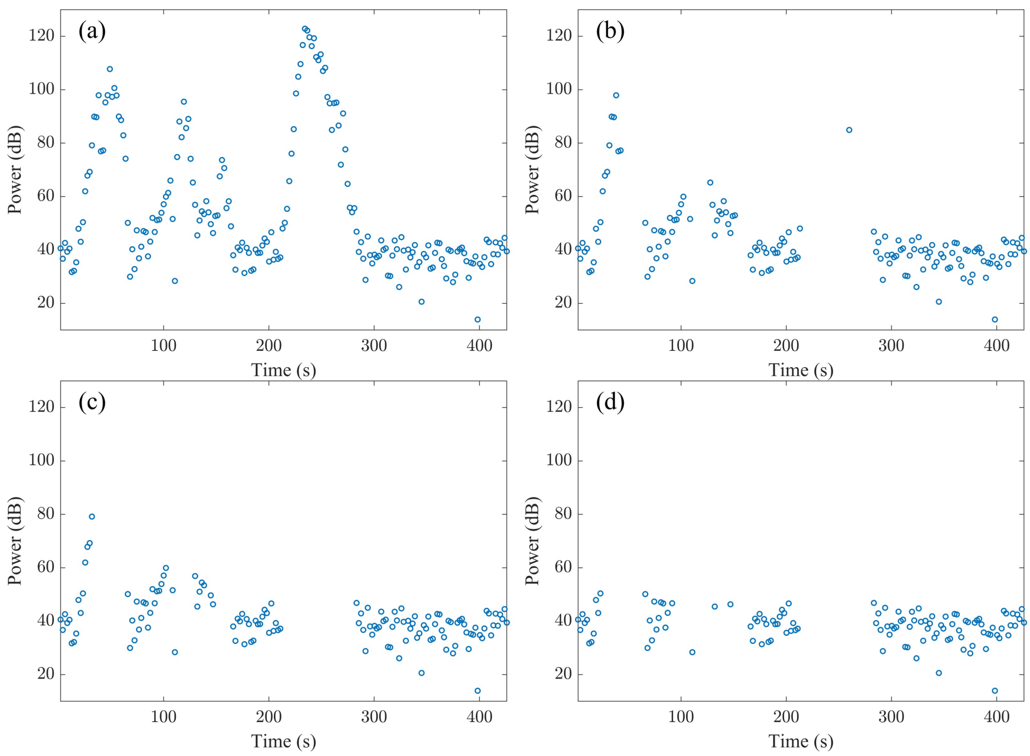

Figure 12. The cancellation process of moving target interference: (**a**) shows the time series before processing, (**b**–**d**) show the time series after the 1st, 2nd, and last processing, respectively.

The time series of this frequency cell before and after moving target interference cancellation is shown in Figure 13. It can be seen that the moving target interference is removed effectively.

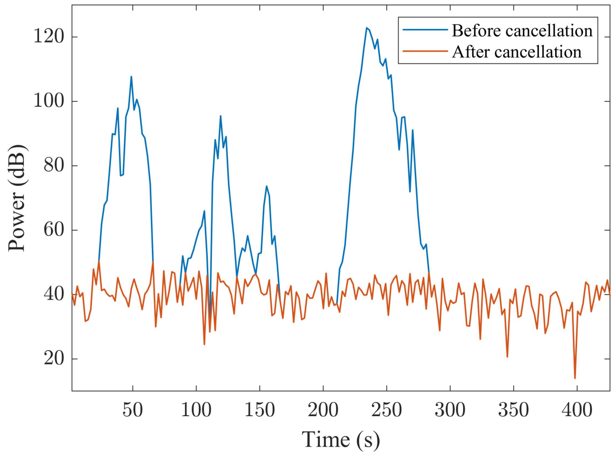

Figure 13. Comparison of the time series before and after moving target interference cancellation at f = 30.99 Hz.

The comparison of the number of iterations required to process this time-Doppler spectrum using the smallest-of selection logic (SO) and the cell-averaging selection logic (CA) is shown in Figure 14. The result proves that the number of iterations required using the smallest-of selection logic is significantly less than that of the cell-averaging selection logic.

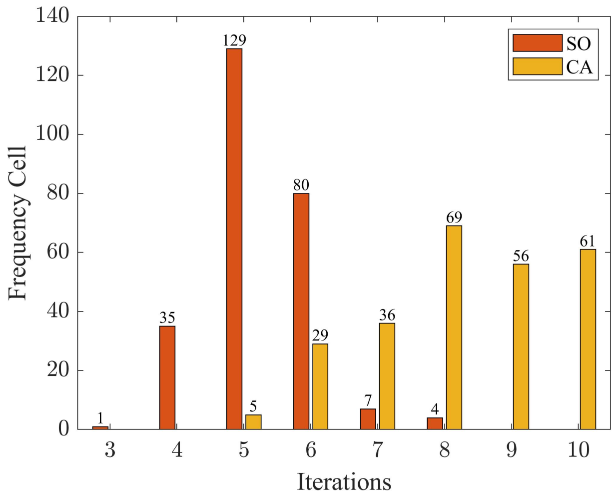

Figure 14. Number of iterations required for the smallest-of selection logic (SO) and the cell-averaging selection logic (CA) to moving target interference cancellation.

The above results show that the smallest-of selection logic can quickly detect moving target interference, and the multi-step deletion scheme can effectively remove moving target interference. Even if moving target interference is severely extended in the time and Doppler dimensions, the proposed CFAR detector can remove it while effectively preserving the Bragg peaks.

3.4. Overall Effect

The time-Doppler spectra at 400 m, 800 m, and 920 m are selected, and the results after ground clutter and moving target interference cancellation are shown in Figure 15. As can be seen from Figure 15, the ground clutter and the moving target interference in the time-Doppler spectra at 400 m, 800 m, and 920 m seriously masked the Bragg peaks. The effectiveness of non-coherent integration is very poor before clutter and interference cancellation, making it difficult to distinguish the Bragg peaks. After processing by the improved phase-based method and CFAR detector proposed in this paper, the ground clutter and moving target interference are removed effectively, and the Bragg peaks are well preserved. The Bragg peaks can be clearly distinguished after non-coherent integration.

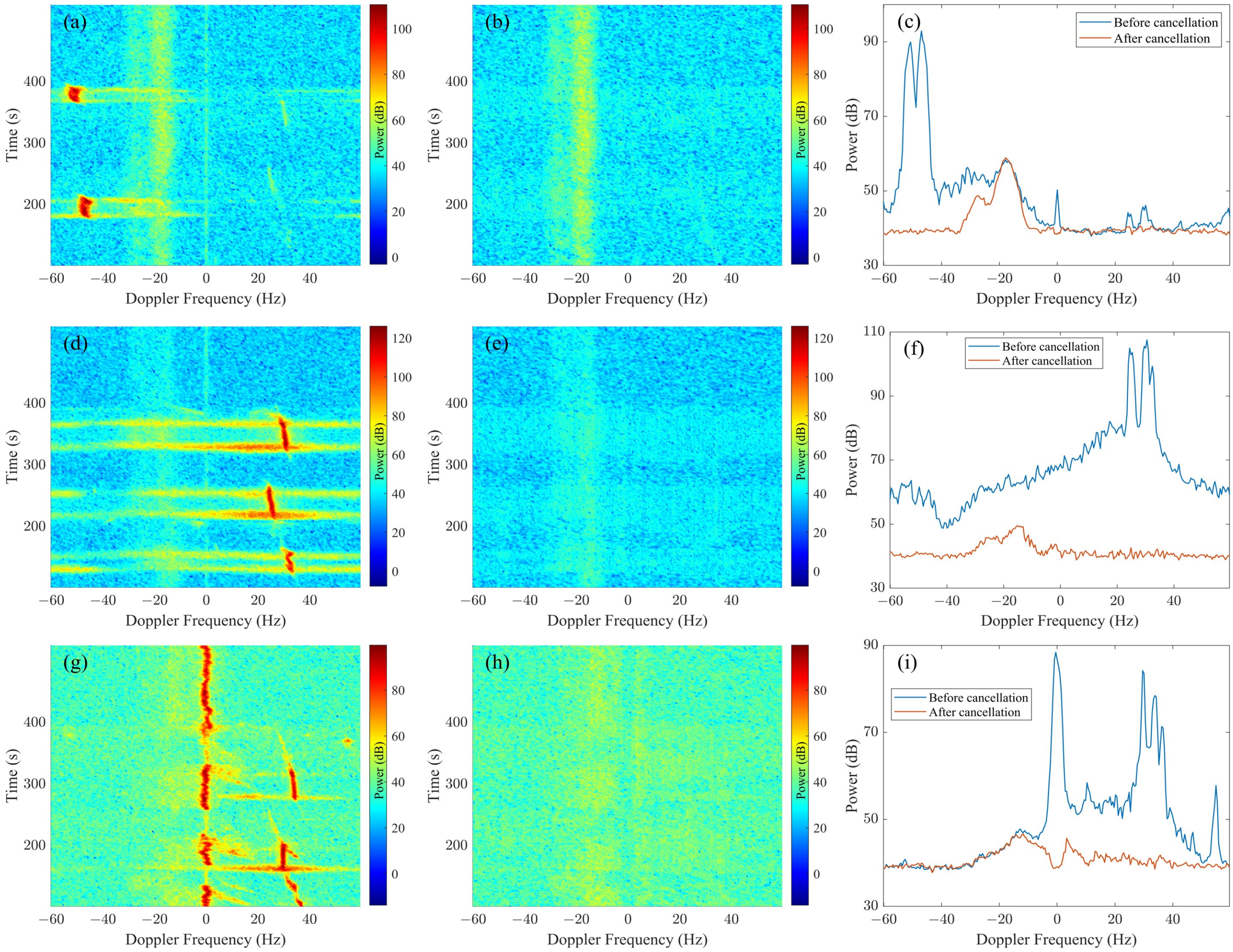

Figure 15. Results of ground clutter and moving target interference cancellation: (**a**,**b**) show the time-Doppler spectra at 400 m before and after cancellation, respectively; (**c**) shows the comparison of the mean Doppler spectra before and after cancellation; (**d**–**f**) are the corresponding results at 800 m, respectively; and (**g**–**i**) are the corresponding results at 920 m, respectively.

4. Discussion

The curve of the Bragg peaks' SNR versus range obtained after clutter and interference cancellation is shown in Figure 16. The area less than 150 m from the radar is in the illumination blind area of the antenna, so the echoes of Bragg waves cannot be received. The more severe attenuation of electromagnetic waves propagating over freshwater than seawater and a smaller wave height dramatically degrade the detection range of radar [35].

Due to the Yangtze River having a width of nearly one thousand meters at the experimental site, the radar is unable to get the entire surface velocity distribution. It can be seen from Figure 16 that the SNR of the Bragg peaks attenuates seriously with range. The coherent S-band radar has an effective detection range of approximately 800 m. When the range exceeds 900 m, the SNR is quite low, making it difficult to extract the river surface velocity.

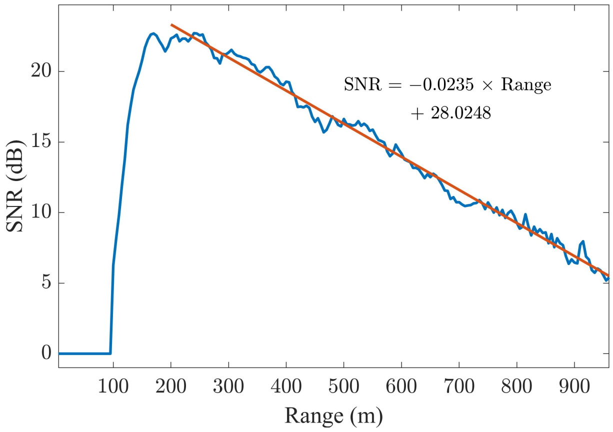

Figure 16. The curve of the Bragg peaks' SNR versus range. The blue line represents the calculated SNR, and the red line represents the fitted curve. The SNR of Bragg peaks attenuates rapidly with range, and the attenuation coefficient obtained by fitting is 23.5 dB/km.

The extraction results of river surface velocity distribution before and after clutter and interference cancellation using the experimental data mentioned above are shown in Figure 17. The extraction result of river surface velocity is biased towards zero due to ground clutter, as shown in Regions II and IV. When the velocity of a cargo ship is consistent with the direction of river flow, the extraction result of river surface velocity would be much larger, as shown in Regions I and III. When the velocity of a cargo ship is opposite to the direction of river flow, the extraction result of river surface velocity would be wrong easily, as shown in Region V. The red oval area in Figure 17 is affected by both ground clutter and moving target interference.

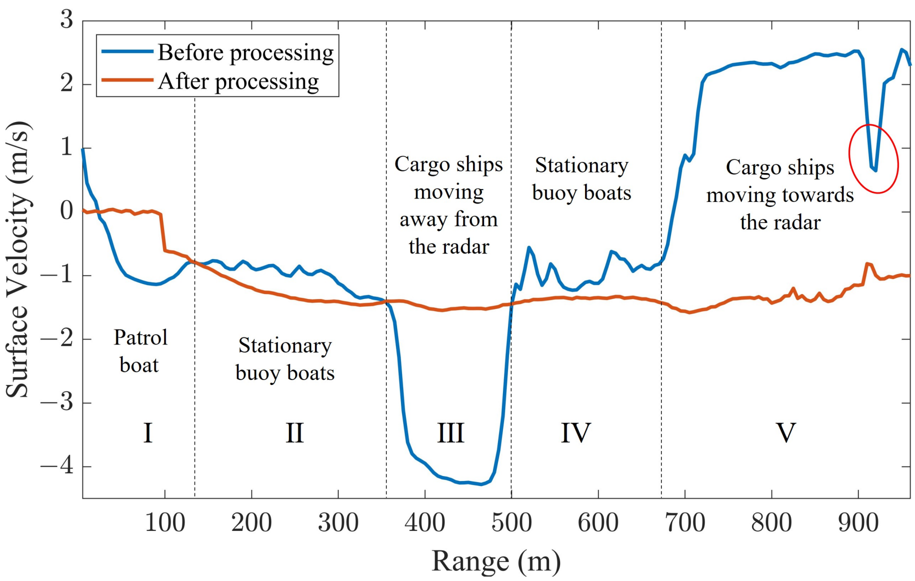

Figure 17. The extraction results of river surface velocity distribution before and after clutter and interference cancellation using the experimental data from 11:40 to 11:49 on July 26.

The extraction results of river surface velocity distribution using the experimental data 3 h later are shown in Figure 18. No cargo ship appeared in channel A, while two appeared in channel B during the period. After processing by the methods proposed in this paper, the river surface velocities of adjacent range cells do not have a large variation, which is consistent with the actual situation. The obtained river surface velocity distribution is more reasonable, indicating that ground clutter and moving target interference are effectively removed.

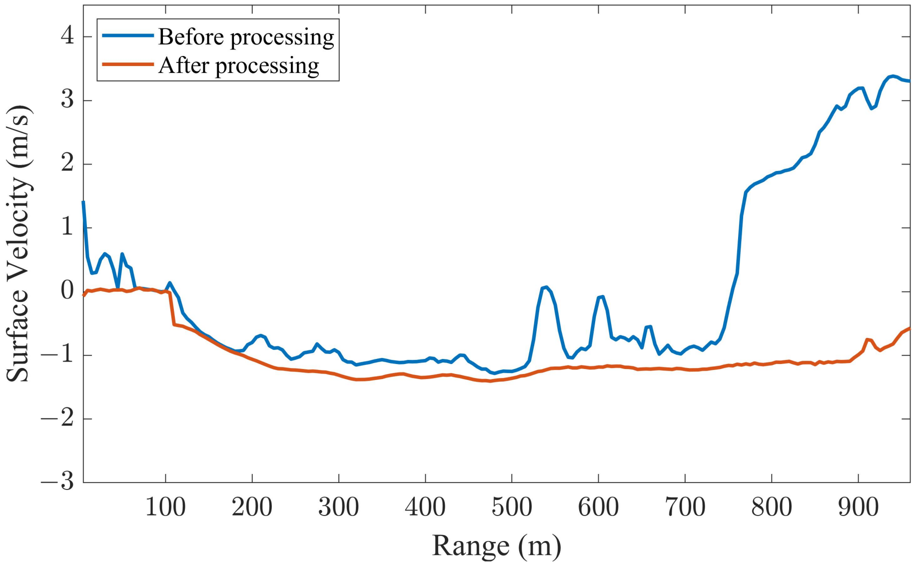

Figure 18. The extraction results of river surface velocity distribution before and after clutter and interference cancellation using the experimental data from 14:40 to 14:49 on July 26.

It can be seen from Figures 17 and 18 that the surface velocity of the Yangtze River is quite low, no more than 2 m/s, which is due to a drought. When measuring a river with a faster surface velocity, the radar's sweep period shown in Table 1 should be reduced, increasing the maximum radial velocity it could measure according to Equation (24). The sweep period of the coherent S-band radar can be reduced to 5.24 ms and 2.64 ms, and the corresponding maximum radial velocities are 5.02 m/s and 9.97 m/s, respectively.

There are some limitations of the methods proposed in this paper. The improved phase-based method relies on the phase difference between ground clutter and noise in the frequency domain. It is difficult to obtain the correct boundaries of ground clutter if the phases of ground clutter are severely disturbed, which can lead to a degradation of ground clutter cancellation. In addition, if the river surface velocity cannot maintain constant for a short period, the improved CFAR detector would remove part of the Bragg peaks. The extraction result would be biased in such a case.

5. Conclusions

This paper proposes two effective methods to remove ground clutter and moving target interference, respectively, in order to measure the surface velocity of rivers with undesired targets.

(1) For ground clutter generated by stationary targets, this paper proposes an improved phase-based method, which eliminates ground clutter after obtaining its boundaries through the phase in the frequency domain. Since ground clutter and noise have different correlations in time, the parameter $\Delta\phi_0$ is calculated first. Then, the method combines it with the product factor a to obtain the boundaries of ground clutter. The value of the parameter $\Delta\phi_0$ in the ground clutter region is solely related to the number of pulses and independent of the spectrum width of ground clutter and other radar parameters. Therefore, the improved phase-based method shows excellent robustness.

(2) For moving target interference generated by moving targets, this paper proposes an improved CFAR detector combining a smallest-of selection logic and a multi-step deletion scheme to detect and remove interference in the time-Doppler spectrum. The detector distinguishes moving target interference through its instability in the time dimension. The use of smallest-of selection logic enables the detector to quickly detect moving target interference. While the combination of a multi-step deletion scheme makes the detector able to eliminate the masking effects caused by the moving target interference which occupies a large number of time cells.

Using the experimental data measuring the surface velocity of the Yangtze River with a coherent S-band radar in July 2022, it is demonstrated that the improved phase-based method and CFAR detector can effectively remove ground clutter and moving target interference, respectively. A more reasonable result of river surface velocity can be extracted after clutter and interference cancellation.

Therefore, the methods proposed in this paper can be used to remove clutter and interference when extracting the surface velocity of rivers with many undesired targets, especially for wide rivers which have rich shipping resources. In the future, we will carry out more experiments and consider the effects of various influencing factors such as wind and rain. Reliable discharge inversion also needs further research.

Author Contributions: Conceptualization, Y.Z. and Z.C.; methodology, Y.Z. and Z.C.; software, Y.Z.; validation, Y.Z., Y.W. and J.H.; formal analysis, Y.Z., Y.W. and J.H.; investigation, Z.C. and C.Z.; resources, Z.C.; data curation, Z.C.; writing—original draft preparation, Y.Z.; writing—review and editing, Z.C. and C.Z.; visualization, Y.Z.; supervision, Z.C.; project administration, Z.C.; funding acquisition, Z.C. All authors have read and agreed to the published version of the manuscript.

Funding: This work was supported in part by the National Natural Science Foundation of China under Grant 42276190.

Data Availability Statement: The authors do not have permission to share data.

Acknowledgments: The authors would like to thank the whole crew of the Jiangxin Water Station for their support with the experiment.

Conflicts of Interest: The authors declare no conflict of interest.

References

1. Plant, W.J.; Keller, W.C.; Hayes, K. Measurement of river surface currents with coherent microwave systems. *IEEE Trans. Geosci. Remote Sens.* **2005**, *43*, 1242–1257. [Crossref] [CrossRef]
2. Bandini, F.; Frías, M.C.; Liu, J.; Simkus, K.; Karagkiolidou, S.; Bauer-Gottwein, P. Challenges with Regard to Unmanned Aerial Systems (UASs) Measurement of River Surface Velocity Using Doppler Radar. *Remote Sens.* **2022**, *14*, 1277. [Crossref] [CrossRef]
3. Yang, Y.; Wen, B.; Wang, C.; Hou, Y. Two-dimensional velocity distribution modeling for natural river based on UHF radar surface current. *J. Hydrol.* **2019**, *577*, 123930. [Crossref] [CrossRef]
4. Lassabatere, L.; Pu, J.H.; Bonakdari, H.; Joannis, C.; Larrarte, F. Velocity distribution in open channel flows: Analytical approach for the outer region. *J. Hydraul. Eng.* **2013**, *139*, 37–43. [Crossref] [CrossRef]
5. Costa, J.E.; Cheng, R.T.; Haeni, F.P.; Melcher, N.; Spicer, K.R.; Hayes, E.; Plant, W.; Hayes, K.; Teague, C.; Barrick, D. Use of radars to monitor stream discharge by noncontact methods. *Water Resour.* **2006**, *42*, 1–14. [Crossref]
6. Herschy R. The velocity-area method. *Flow Meas. Instrum.* **1993**, *4*, 7–10. [CrossRef]
7. Cheng, R.T.; Gartner, J.W. Complete velocity distribution in river cross-sections measured by acoustic instruments. In Proceedings of the IEEE/OES Seventh Working Conference on Current Measurement Technology, San Diego, CA, USA, 13–15 March 2003; pp. 21–26. [Crossref]
8. Gunawan, B.; Sterling, M.; Knight, D.W. Using an acoustic Doppler current profiler in a small river. *Water Environ. J.* **2009**, *24*, 147–158. [Crossref] [CrossRef]
9. Fulton, J.W.; Mason, C.A.; Eggleston, J.R.; Nicotra, M.J.; Chiu, C.L.; Henneberg, M.F.; Best, H.R.; Cederberg, J.R.; Holnbeck, S.R.; Lotspeich, R.R.; et al. Near-Field Remote Sensing of Surface Velocity and River Discharge Using Radars and the Probability Concept at 10 U.S. Geological Survey Streamgages. *Remote Sens.* **2020**, *12*, 1296. [Crossref] [CrossRef]
10. Teague, C.C.; Barrick, D.E.; Lilleboe, P.M.; Cheng, R.T. Initial river test of a monostatic RiverSonde streamflow measurement system. In Proceedings of the IEEE/OES Seventh Working Conference on Current Measurement Technology, San Diego, CA, USA, 13–15 March 2003; pp. 46–50. [Crossref]
11. Teague, C.C.; Barrick, D.E.; Lilleboe, P.M.; Cheng, R.T.; Ruhl, C.A. UHF RiverSonde Observations of Water Surface Velocity at Threemile Slough, California. In Proceedings of the IEEE International Geoscience and Remote Sensing Symposium, Seoul, Republic of Korea, 29–29 July 2005; pp. 4383–4386. [Crossref]
12. Teague, C.C.; Barrick, D.E.; Lilleboe, P.M.; Roarty, H.; Holden, D.; Goldinger, D. Extended-range RiverSonde operation on the Hudson River. In Proceedings of the 2011 IEEE/OES 10th Current, Waves and Turbulence Measurements (CWTM), Monterey, CA, USA, 20–23 March 2011; pp. 78–80. [Crossref]
13. Plant, W.J.; Keller, W.C.; Siani, C.; Chatham, G. River Current Measurement Using Coherent Microwave Radar: Toward Gaging Unstable Streams. In Proceedings of the 2008 IEEE/OES 9th Working Conference on Current Measurement Technology, Charleston, SC, USA, 17–19 March 2008; pp. 245–249. [Crossref]

14. Plant, W.J.; Keller, W.C.; Hayes, K.; Contreras, R. Measurement of river surface currents using rough surface scattering. In Proceedings of the 2005 IEEE Antennas and Propagation Society International Symposium, Washington, DC, USA, 3–8 July 2005; pp. 380–383. [Crossref]
15. Wang, C.; Wen, B.; Ma, Z.; Yan, W.; Huang, X. Measurement of River Surface Currents with UHF FMCW Radar Systems. *J. Electromagn. Waves Appl.* **2007**, *21*, 375–386. [Crossref] [CrossRef]
16. Yang, Y.; Wen, B.; Wang, C.; Hou, Y. Real-Time and Automatic River Discharge Measurement with UHF Radar. *IEEE Geosci. Remote Sens. Lett.* **2020**, *17*, 1851–1855. [Crossref] [CrossRef]
17. Phyu, H.P.; Lwin, K.S.; Oo, T.T.; Aung, P.T. Analysis on Ground Clutter Mitigation Using IIR Filter and Frequency Domain Filters for C-Band Phased Array Weather Radar. In Proceedings of the 2020 International Conference on Advanced Information Technologies (ICAIT), Yangon, Myanmar, 4–5 November 2020; pp. 48–52. [Crossref]
18. Siggia, A.D.; Passarelli, R.E. Gaussian model adaptive processing (GMAP) for improved ground clutter cancellation and moment calculation. In Proceedings of the Third European Conference on Radar in Meteorology and Hydrology ERAD, Visby, Sweden, 6–10 September 2004; pp. 67–73.
19. Ice, R.L.; Rhoton, R.D.; Saxion, D.S.; Ray, C.A.; Patel, N.K.; Warde, D.A.; Free, A.D.; Boydstun, O.E.; Berkowitz, D.S.; Chrisman, J.N.; et al. Optimizing clutter filtering in the WSR-88D. In Proceedings of the 23rd Intercontinental Conference Interactive Information Processing Systems (IIPS) Meteorology Oceanography Hydrology, Boston, MA, USA, 14–18 January 2007.
20. Warde, D.A.; Torres, S.M. The Autocorrelation Spectral Density for Doppler-Weather-Radar Signal Analysis. *IEEE Trans. Geosci. Remote Sens.* **2014**, *52*, 508–518. [Crossref] [CrossRef]
21. Torres, S.M.; Warde, D.A. Ground clutter mitigation for weather radars using the autocorrelation spectral density. *J. Atmos. Oceanic Technol.* **2014**, *31*, 2049–2066. [Crossref] [CrossRef]
22. Golbon-Haghighi, M.; Zhang, G.; Doviak, R.J. Ground Clutter Detection for Weather Radar Using Phase Fluctuation Index. *IEEE Trans. Geosci. Remote Sens.* **2019**, *57*, 2889–2895. [Crossref] [CrossRef]
23. Wang, Y.; Wu, D.; Yu, Q.; Zhu, D.; Meng, F. A weather signal detection algorithm based on EVD in elevation for airborne weather radar. *Digital Signal Process.* **2021**, *116*, 103118. [Crossref] [CrossRef]
24. Bachmann, S.M. Phase-Based Clutter Identification in Spectra of Weather Radar Signals. *IEEE Geosci. Remote Sens. Lett.* **2008**, *5*, 487–491. [Crossref] [CrossRef]
25. Weiss, M. Analysis of some modified cell-averaging CFAR processors in multiple-target situations. *IEEE Trans. Aerosp. Electron. Syst.* **1982**, *18*, 102–114. [Crossref] [CrossRef]
26. Barboy, B.; Lomes, A.; Perkalski, E. Cell-averaging CFAR for multiple-target situations. *IEE Proc. F Commun. Radar Signal Process.* **1986**, *133*, 176–186. [Crossref] [CrossRef]
27. Xu, C.; Li, Y.; Ji, C.; Huang, Y.; Wang, H.; Xia, Y. An improved CFAR algorithm for target detection. In Proceedings of the 2017 International Symposium on Intelligent Signal Processing and Communication Systems (ISPACS), Xiamen, China, 6–9 November 2017; pp. 883–888. [Crossref]
28. Zhang, W.; Li, H.; Sun, G.; He, Z. Enhanced Detection of Doppler-Spread Targets for FMCW Radar. *IEEE Trans. Aerosp. Electron. Syst.* **2019**, *55*, 2066–2078. [Crossref] [CrossRef]
29. Kuang C.; Wang, C.; Wen, B.; Hou, Y.; Lai, Y. An improved CA-CFAR method for ship target detection in strong clutter using UHF radar. *IEEE Signal Process. Lett.* **2020**, *27*, 1445–1449. [Crossref] [CrossRef]
30. Plant, W.J.; Keller, W.C. Evidence of Bragg scattering in microwave Doppler spectra of sea return. *J. Geophys. Res.* **1990**, *95*, 16299–16310. [Crossref] [CrossRef]
31. Alimenti, F.; Bonafoni, S.; Gallo, E.; Palazzi, V.; Gatti, R.V.; Mezzanotte, P.; Roselli, L.; Zito, D.; Barbetta, S.; Corradini, D.; et al. Noncontact Measurement of River Surface Velocity and Discharge Estimation With a Low-Cost Doppler Radar Sensor. *IEEE Trans. Geosci. Remote Sens.* **2020**, *58*, 5195–5207. [Crossref] [CrossRef]
32. Chen, Z.; Wang, Z.; Chen, X.; Zhao, C.; Xie, F.; He, C. S-band Doppler wave radar system. *Remote Sens.* **2017**, *9*, 1302. [Crossref] [CrossRef]
33. Zhao, C.; Wang, X.; Chen, Z.; Wu, S.; Zeng, Y. Inversion of Wave Parameters From Time-Doppler Spectrum Using Shore-Based Coherent S-Band Radar. *IEEE Trans. Geosci. Remote Sens.* **2023**, *61*, 1–11. [Crossref] [CrossRef]
34. Teague, C.C.; Barrick, D.E.; Lilleboe, P.; Cheng, R.T. Canal and river tests of a RiverSonde streamflow measurement system. In Proceedings of the IEEE 2001 International Geoscience and Remote Sensing Symposium, Sydney, Australia, 9–13 July 2001; pp. 1288–1290. [Crossref]
35. Fernandez, D.M.; Meadows, L.A.; Vesecky, J.F.; Teague, C.C.; Paduan, J.D.; Hansen, P. Surface current measurements by HF radar in freshwater lakes. *IEEE J. Ocean. Eng.* **2000**, *25*, 458–471. [Crossref] [CrossRef]